small methods
www.small-methods.com

Printing Crack-Free Microporous Structures by Combining Additive Manufacturing with Colloidal Assembly

*Benedikt F. Winhard, Laura G. Maragno, Alberto Gomez-Gomez, Julian Katz, and Kaline P. Furlan**

To date high printing resolution and scalability, i.e., macroscale component dimensions and fast printing, are incompatible characteristics for additive manufacturing (AM) processes. It is hereby demonstrated that the combination of direct writing as an AM process with colloidal assembly enables the breaching of this processing barrier. By tailoring printing parameters for polystyrene (PS) microparticle-templates, how to avoid coffee ring formation is demonstrated, thus printing uniform single lines and macroscale areas. Moreover, a novel "comb"-strategy is introduced to print macroscale, crack-free colloidal coatings with low viscous colloidal suspensions. The printed templates are transformed into ceramic microporous channels as well as photonic coatings via atomic layer deposition (ALD) and calcination. The obtained structures reveal promising wicking capabilities and broadband reflection in the near-infrared, respectively. This work provides guidelines for printing low viscous colloidal suspensions and highlights the advancements that this printing process offers toward novel applications of colloidal-based printed structures.

1. Introduction

The implementation of additive manufacturing (AM) processes into production routes is consistently expanding. To date, there is an ever-increasing interest to apply AM processes in various industries, such as construction,[1] biomedicine,[2] or aerospace.[3] The latter offers a variety of AM applications itself: Next to lightweight structural components, there is a demand for novel heat management strategies that enhance the overall efficiency of aerospace vehicles.[4] For instance, high-power electronics in aerospace vehicles become continuously smaller, run longer cycles, and require higher power, which must eventually be compensated with more sophisticated heat management strategies.[4] Here, on-chip microfluidics could aid to effectively remove heat.[4] This requires processing techniques with great design and material flexibility. However, current processes for microfluidics rely mainly on lithography techniques, which are limited in materials selection and restricted to rather 2D designs.[5] Hence, the development of novel processing routes is required that allow design flexible processes such as AM and greater materials variety.[4]

Next to thermal management in high-power electronics, thermal shielding in high-temperature applications requires consistent enhancement toward higher working temperatures: here, next-generation reflective thermal barrier coatings (rTBCs) with tailored microstructures have lower thermal conductivity in comparison to traditional TBCs,[6] but most importantly are capable of additionally scatter heat radiation.[7] The emittance of heat radiation scales with temperature by T^4, hence obstructing radiative heat transport becomes very relevant with increasing working temperatures (>1000 °C). Therefore, coating components for high-temperature applications with such rTBCs could allow the devices to work at higher operating temperatures.

Both, microfluidics as well as rTBCs require feature sizes in the submicron and micron scales, but simultaneously comprise macroscopic dimensions.[4,7] AM processes such as two-photon polymerization enable printing in the submicron scale; however, lack in scalability due to their slow printing speed as well as high equipment and resin costs, which usually limit the printed structures to submillimeter dimensions.[8] Hence, overcoming the trade-off between printing resolution and scalability requires novel printing approaches. Combining direct writing as extrusion-based AM process with colloidal assembly, which we refer to as AMCA (Additive Manufacturing combined with Colloidal Assembly) process,[9] links the so far incompatible process characteristics. While direct writing allows for printing macroscale structures, tailored colloidal assembly within the extrudate during printing enhances the printing resolution to the submicron scale.

This printing approach and similar ones exploiting inkjet printing[10] have gained more and more attention in recent years.[11–15] Initially, Tan et al.[14] printed free-standing columns via direct writing made from submicron-sized, monodisperse polystyrene , gold or silica particles. The obtained columns

B. F. Winhard, L. G. Maragno, A. Gomez-Gomez, J. Katz, K. P. Furlan
Hamburg University of Technology
Institute of Advanced Ceramics
Integrated Materials Systems Group
Denickestraße 15, 21073 Hamburg, Germany
E-mail: kaline.furlan@tuhh.de

The ORCID identification number(s) for the author(s) of this article can be found under https://doi.org/10.1002/smtd.202201183.

DOI: 10.1002/smtd.202201183

were polycrystalline and exhibited iridescent structural coloration. To print geometries with non-iridescent, angular independent structural coloration, others[11,13] continued the approach by adding a viscous polymer phase to the suspension. Thereby, ordering of the colloids is impeded, which forms an amorphous particle assembly, i.e., a photonic glass (PhG) structure.[11,13] The presence of a polymeric phase; however, limits the functionality and applicability of the obtained colloidal structures to that of the polymeric phase, e.g. low-temperature stability, low-chemical resistance, as well as low strength and stiffness. In a second study, Tan et al.[15] printed single lines on flat surfaces without an additional polymeric phase. Here, however, a severe coffee ring effect (CRE) can be seen in the final structures. The CRE is an ubiquitous phenomenon when exploiting evaporation-induced colloidal assembly and was initially described by Deegan et al.[16] During solvent evaporation, a capillary flow is induced that is directed toward the contact line of a fluid deposit. The induced flow transports particles to the periphery, thus obstructing uniform particle deposition. We demonstrated in a preceding study,[9] that the CRE can be prevented for PS microparticle droplets by reducing the dispense volume. This approach however, brings limitations in regard to total printing time for macroscale areas.

In this work, we developed macroscale line and area printing of colloidal suspensions with the AMCA process. We demonstrate that the CRE can be prevented in single lines correspondingly to the previous approach,[9] but only with proper tailoring of the particle concentrations and adjustment of printing velocities. Moreover, we further developed the AMCA process to print macroscopic homogenous areas of crack-free particle assemblies. In this regard, we demonstrate that the common line-by-line approach for area printing is inapplicable for direct writing of low viscous suspensions and thus, for AMCA. Instead, we introduce a novel "comb"-strategy that allows to coat macroscopic areas with colloids within minutes. The printed PS-templates were post-processed via atomic layer deposition (ALD) and finally calcinated, thus forming functional ceramic microporous channels and layers. The wicking capabilities and reflection capabilities were assessed, respectively, to demonstrate the potential application of the fabricated structures in microfluidics and high-temperature applications. This work highlights the disruptive combination of submicron scale feature sizes and scalability of components' dimensions that the AMCA process facilitates, which paths the way to novel applications of colloidal structures.

2. Results and Discussion

2.1. Printing PS-Templates

2.1.1. Single Line Printing

The two printing velocities, i.e., writing velocity v_W and dispense velocity v_D, must be set to a certain velocity ratio v_W/v_D, to successfully print straight single lines via direct writing with low viscosity colloidal suspensions. Here, the writing velocity v_W refers to the velocity of the needle in relation to the substrate surface. The dispense velocity v_D is defined as the suspension's

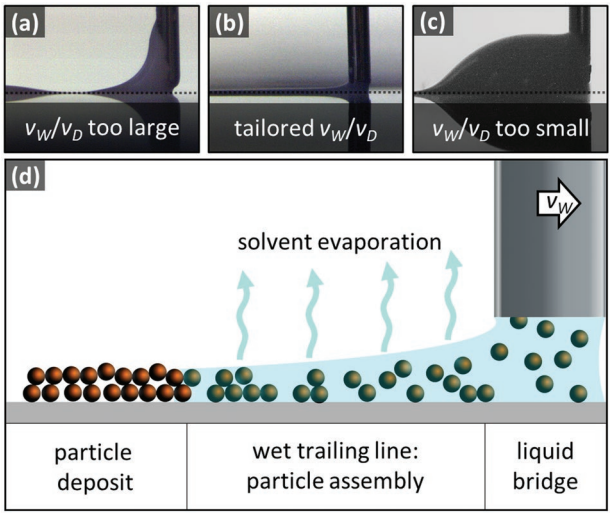

Figure 1. In situ high-resolution snapshots of the AMCA printing process with different parameters, namely a) low v_W/v_D ratio, b) matching v_D and v_W, and c) high v_W/v_D ratio. v_W stands for writing velocity, while v_D stands for dispense velocity. d) Schematic cross-sectional drawing of a line printing process subdivided into zones from right to left: needle tip and liquid bridge; trailing "wet"-line region; and dry particle deposit.

velocity at the needle tip: $v_D = v_P\ A_P\ /\ A_N = v_P d_P^2\ /\ d_N^2$, where v_P is the plunger velocity set by the linear stage; A_P and d_p the cross-section and diameter of the plunger; A_N and d_N the cross-section as well as diameter of the needle tip. Since the entire needle surface was wetted during printing, d_N is the outer needle diameter. The velocity ratio v_W/v_D for printing straight lines is not only but foremost dependent on the suspension and substrate properties, which are discussed later. When exceeding a critical ratio, the printed line splits up into equidistant sessile droplets (**Figure 1**a). A droplet forms at the needle tip that gets dragged over the substrate surface due to the small adhesion of the contact line with the substrate and eventually unpins from the needle tip. Conversely, setting the ratio v_W/v_D too small results in bulging of the trailing line (Figure 1c). This phenomenon has already been observed in other extrusion-based AM techniques.[17,18,19] Duineveld and co-workers[17] explain this effect by an increasing pressure at the needle tip in relation to the existent internal pressure in the wet printed line. The higher pressure originates from a locally higher contact angle θ. The contact angle gets equilibrated by line broadening, but at the same time by an internal flow Q_i that is directed against the writing direction and may eventually cause a bulge.[18] Hence, it is crucial to adjust the velocity ratio v_W/v_D to avoid both: lines splitting up into single droplets as well as lines bulging after extrusion. For the suspensions investigated in this work, straight single lines were printed with velocity ratios between 17 and 170. At such conditions, a stable liquid bridge forms between the needle tip and the substrate surface. The size of the liquid bridge not only depends on the distance between the needle tip and the substrate surface but also on the wettability of the suspension on the substrate and on the wettability of the suspension on the needle tip. In our experiments, we kept the distance between the needle and substrate constant at 50 µm. The contact angle of the suspension on the sapphire substrate

was ≈84°, as determined in our previous work,[9] while the surface of the needle tip was wetted entirely during printing. Therefore, the width of the liquid bridge was about the size of the outer diameter of the needle tip for our printing setup.

Aside from the stability of the contact line, the structural ordering of the particles during the self-assembly was also explored. In a study by Tan et al.[15] ordered structures, there named colloidal crystals, were printed via a similar approach exploiting direct writing. To achieve long-range order, the writing speed was adjusted to the self-assembly rate of the crystal. In our work, we aimed to develop amorphous structures, rather than often-investigated crystalline structures. The reason for that is the proven better performance in terms of radiation reflection over a broadband range for disordered, PhGs, than ordered, photonic crystal structures.[6,7] Therefore, in our work the writing velocity is not restricted to the crystal growth rate. Instead, we aimed for faster writing velocities to achieve amorphous particle assemblies. By increasing the writing velocity, less suspension is deposited per printed length Δl_L, hence the printed line dries faster. Particles require however a minimum amount of time t_D to form an ordered assembly via Brownian motion, which scales with the particle radius $\approx R_P{}^2$.[20] By printing with writing velocities of at least 1 mm s^{-1}, in our experiments the particles could not order during solvent evaporation, thus we achieved amorphous particle assemblies. The fast printing velocities led not only to a different particle deposition than in previous work by Tan et al.[15] but also a different printing process: The steady printing condition of the process can be subdivided in three spatial zones—the liquid bridge at the needle tip, a wet trailing line behind the liquid bridge, and the dried amorphous particle deposit (Figure 1d).

By printing with a writing velocity v_W of 1 mm s^{-1}, the dispense rate of the suspension exceeded the evaporation rate of the solvent. Hence, a wet line was formed that was trailing the needle. The wet trailing line splits up into equally sized equidistant single droplets, because the deposited suspension tends to lower its surface-to-volume ratio, which can be described by a surface tension force F_S that is directed normal to the wet lines surface and toward the line center. This causes the contact line to recede,[21] i.e., the contact line is unable to remain pinned to the substrate. To be able to print a continuous straight wet line, the contact line must be pinned during the entire solvent evaporation. The presence of PS particles at the contact line can create an adhesion force F_A that can pin the particles as well as the contact line.[22] Such adhesion is related to the electrostatic and Van der Waals forces (F_E and F_{VDW}, respectively) between particles and substrate. Moreover, drag forces F_D induced by the capillary flow of the solvent and the vertical component of the surface tension force F_S, which acts on the outmost PS particles,[22] aid pinning of the contact line. A mathematical model by Yu et al.[23,24] describes this contact line pinning mechanism of microparticles taking all aforementioned forces into account. Based on this model for line pinning, it becomes evident that PS particles must adhere at the contact line immediately right after extrusion to be able to keep a printed wet trailing line straight. In fact, particles migrate toward the contact line as soon as the solvent evaporates, because the evaporation induces a capillary flow that is directed outward to the line rim, thereby exerting a drag force F_D on the particles, which aids pinning of the contact line (**Figure 2**a).[16] However, the presence of just a few particles at the contact line, as schematically indicated in Figure 2a, does not suffice to be able to pin the contact line. In reality, the net drag force $F_{D,net}$ and adhesion force $F_{A,net}$ increases with the number of particles at the contact line, due to the additional contributions of each particle:[23] $F_{D,net} = nF_D$ and $F_{A,net} = n(F_{VDW} + F_E)$, where n is the number of particles. Based on optical images of our dried deposits (Figure 2c), an average of about four particles was required at the contact line in our experiments to maintain pinning and enable the printing of straight lines. This limited the dispense velocity v_D to a minimum of 5.9 µm s^{-1}. For slower dispense velocities and thereby larger velocity ratios v_W/v_D, too few particles were dispensed leading to an unstable printing condition described earlier (Figure 1a). Moreover, a limit for the writing velocity was determined to be $v_W = 1$ mm s^{-1} when writing with a minimum v_D of 5.9 µm s^{-1}. Faster v_W led to the split up of the wet line into single droplets, because too few particles could settle at the contact line, which could not keep it pinned.

In case a stable printing condition is used, the PS particles continuously migrate toward the pinned contact line, transverse to the printing direction, while the solvent evaporates (Figure 2a). However, such behavior leads to particles accumulating at the contact line, thus forming the well-known CRE. Nonetheless, to enable future applications in microfluidic systems or for area printing, a CRE-free homogenous particle distribution is necessary. Hence, to get rid of the CRE, we transferred the previous knowledge from our work of droplet printing regarding a surface capturing effect to prevent CRE[9] into line printing by reducing the cross-sectional dimensions of our wet lines. To apply this approach, we used the 2D cross-sectional view of the lines to describe the major motion direction of particles, i.e., toward the contact line. The resulting 2D shape for both, droplets and wet lines can be described by a circular segment, if the dimensions are smaller than the capillary length $L_c = \sqrt{\gamma / \rho g}$ of the solvent, where γ is the surface tension, ρ is the density of the liquid and g the gravitational acceleration.[25] The L_c for water is ≈2.7 mm, hence our printed lines (max. line width $w_L = 0.5$ mm) had dimensions that could be related to the cross-sectional shape of a small droplet, represented by the circular segment in Figure 2c top.

To be able to reduce the dimensions of this circular segment shape in a line printing process, we reduced the dispense velocity v_D at a constant writing velocity v_W of 1 mm s^{-1}. As can be seen in the line profiles of the dried printed particle deposits (Figure 2b), reducing the dispense velocity lowered indeed the formation of the CRE. For $v_D = 59.1$ µm s^{-1} an accumulation of particles at the contact lines can be clearly recognized based on the height increase of the line profile toward the periphery as well as the bright grey contours of the line in the optical image (Figure 2c). This particle accumulation at the contact lines became gradually less for lower dispense velocities (Figure 2b). With decreasing dispense velocity, the CRE formation during particle assembly was prevented completely, however incomplete surface coverage is achieved, as demonstrated for $v_D = 5.9$ µm s^{-1} (Figure 2c). The initial cross-sectional area of the wet lines after extrusion A_i can be calculated from the printing velocities as follows, assuming no internal flows in printing direction and no solvent evaporation:

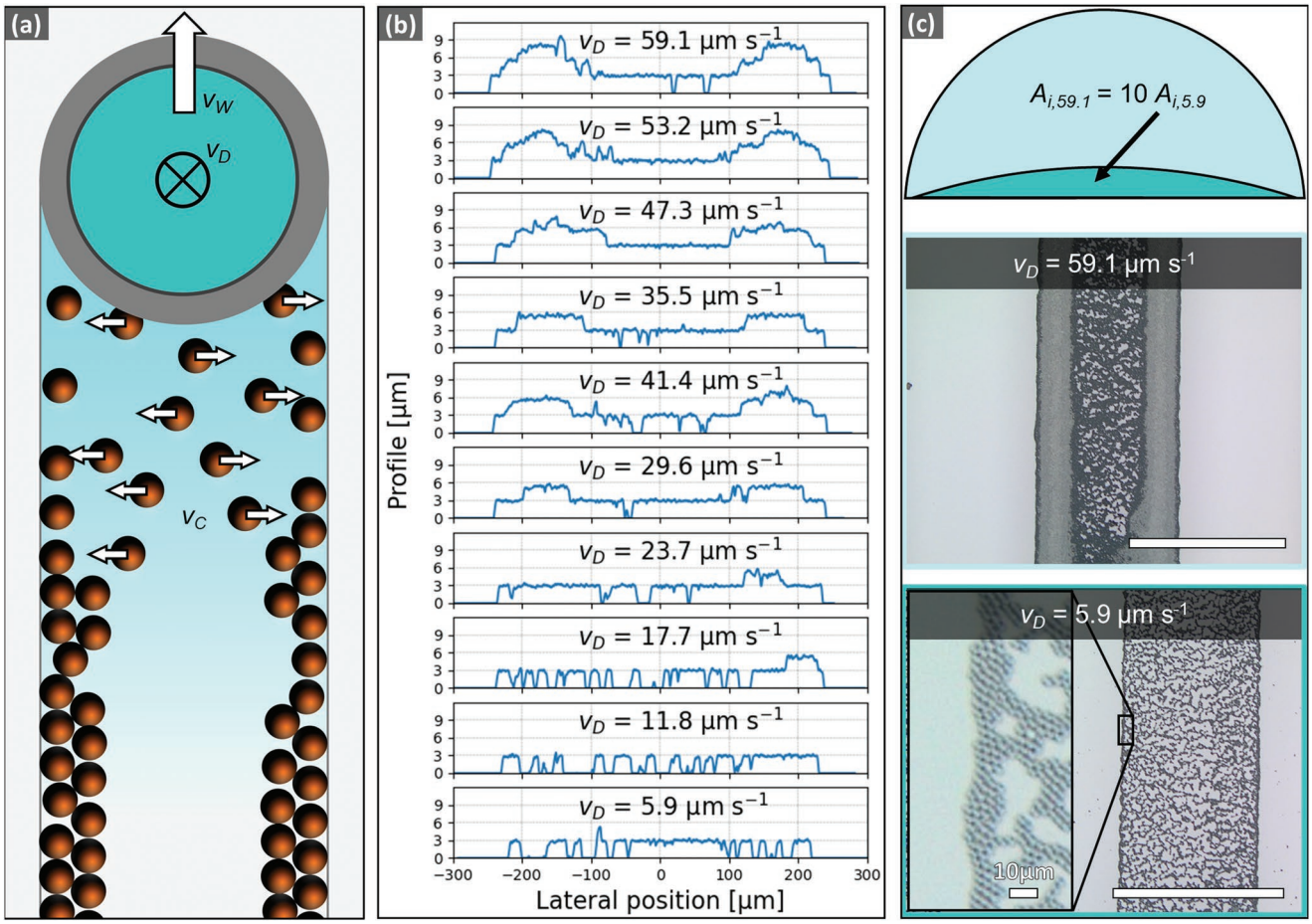

Figure 2. a) Schematic drawing of a line printing from top view: The needle moves upwards while dispensing suspension onto the substrate (black cross indicates flow direction of suspension in needle). The particles in the wet trailing line migrate with velocity v_C to the contact line due to solvent evaporation, thus ensure pinning of the contact line, but also can form a CRE. b) Line profiles for various v_D (constant v_W = 1 mm s^{-1}). c) Scheme of wet lines' cross-sections printed with v_D = 59.1 and 5.9 µm s^{-1}, and optical images illustrating the particle distribution in dried lines for both labelled dispense velocities. For v_D = 5.9 µm s^{-1} an additional inset shows the particle distribution at the line edge. In the optical images, particles are shown in gray and dark gray, while the substrate shows a whitish milky color. Scale bars represent 500 µm.

$$A_i = \frac{A_N v_D}{v_W} \quad (1)$$

Hence, decreasing the dispense velocity by one magnitude (from 59.1 to 5.9 µm s^{-1}), consequently reduces the initial cross-section of the wet trailing lines according to: $A_{i,vD59.1}$ = 10 $A_{i,vD5.9}$. Similar to the previous study on single droplets,[9] a smaller cross-section lead to an average shorter evaporation time. However, the minimum distance l_c that the particles must travel within the timeframe of solvent evaporation to form a CRE stays constant for different v_D, as it can be defined as the average distance between two particles in the suspension:[9,26] $l_c = R_P \sqrt[3]{4\,\pi\,\rho_P / 3\,c}$, where R_P is the radius of the particles, ρ_P is the particle density and c the particles' solid concentration. Hence, by reducing the dispense velocity, the evaporation time becomes shorter, whereas the migration distance l_c stays constant. This effect reduces particle migration toward the contact line, thus successfully preventing the CRE without the need for, e.g., surfactants,[27] hydrophobic substrates,[28] pH,[29] or temperature modification[30] as exploited in other studies.

Noteworthy, the line width of the dried deposits remained almost constant at an average width of 0.476 mm (0.015 mm standard deviation), when reducing v_D. Additionally, the width of 0.476 mm corresponds to the outer diameter of the needle tip, which demonstrates that the contact line was pinned immediately after extrusion. Hence, the width of the wet trailing line and final particle deposit was defined by the width of the liquid bridge.

As mentioned previously, although the CRE was suppressed for v_D = 5.9 µm s^{-1}, the dried lines exhibited patchy particle assemblies. Densely filled lines are however required to be able to fulfill application as templates for microfluidic channels or TBCs (See details in Sections 2.2.1 and 2.2.2). To adjust the particles' packing fraction in the printed lines, the particles' solid concentration in the suspension was additionally varied between 50 and 350 mg mL^{-1}, thus a 2D parameter space of v_D and c was investigated (**Figure 3**a).

For the lowest particle concentration c = 50 mg mL^{-1}, the contact line could not be pinned for any investigated dispense speed, thus no lines could be printed. At 100 and 150 mg mL^{-1}

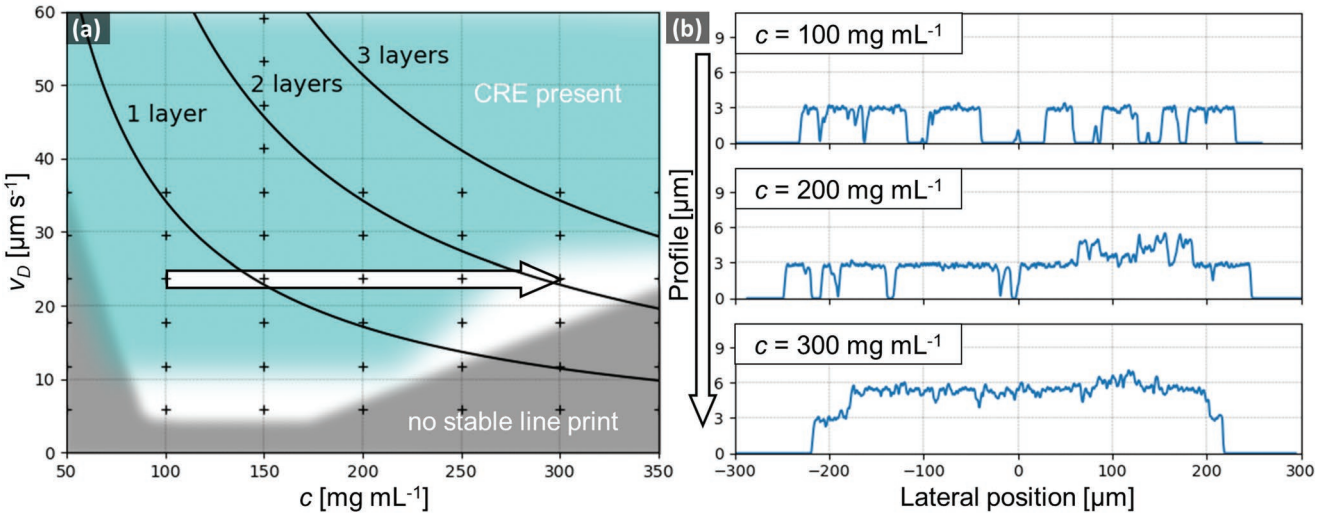

Figure 3. a) Operational phase diagram of dispense speed over particle concentration. Black "+"-marks display investigated parameter sets. Writing speed v_W was kept constant at 1 mm s^{-1}. Solid black curves illustrate required dispense speed and particle concentration to print line with one, two, and three layers of particles based on the analytical model of Equation 2. Turquoise area depicts printing conditions that form a CRE; grey area covers printing conditions where lines could not be printed continuously. White arrow in the phase diagram marks parameter window, from which in (b) three cross sectional profiles of correspondingly printed lines are displayed.

the printing conditions were stable up to a minimum v_D = 5.9 µm s^{-1}. However, the printed lines were not completely filled with particles or formed a CRE for higher dispense speeds as described earlier. By further increasing the particle concentration, the minimum dispense velocity increased gradually from 5.9 µm s^{-1} for 150 mg mL^{-1} to 23.7 µm s^{-1} for 350 mg mL^{-1}. Dispense velocities below these limits resulted in line thinning and eventually breakup of the liquid bridge. The increase in particle concentration lowers the volume fraction of the solvent in the suspension from 90 to 67 vol.% for 100 and 350 mg mL^{-1}, respectively. This decrease in solvent volume fraction reduces the dispense rate of just the solvent to the extent that it becomes less than the evaporation rate, thereby thinning and rupturing the liquid bridge. Due to faster evaporation with higher particle concentration c not only the minimum v_D for stable line printing increased, but so did the maximum v_D for CRE-free lines (Figure 3a). Whereas CRE could only be prevented with v_D = 5.9 µm s^{-1} for c = 150 mg mL^{-1}, at 300 mg mL^{-1} particle concentration, the CRE could be avoided even for dispense velocities as fast as v_D = 23.7 µm s^{-1}. For c = 300 mg mL^{-1} and v_D = 23.7 µm s^{-1} uniform dense CRE-free lines consisting of two particle layers were printed (Figure 3b). To predict the required velocity ratio v_W/v_D for a certain particle concentration to print dense lines with a certain number of particle layers, we propose the following model (detailed calculation steps can be found in the Supplementary Information):

$$\frac{v_W}{v_D} = \frac{3\,c\,A_N}{4\,w_L\,\rho_P\,R_P\,f\,l} \quad (2)$$

where f is the packing fraction and l is the number of particle layers. For our particle assemblies, we assumed a packing fraction f = 0.64, which is the highest fraction for an amorphous packing of monodisperse spheres.[31] Moreover, to apply the model to our investigated parameter space, we set the line width w_L to the experimental average width of 0.476 mm, ρ_P = 1.05 g cm^{-3}, R_P = 1.5 µm, and A_N = 0.176 mm^2. We calculated the required dispense velocity for various concentrations to print lines with one, two, and three particle layers with Equation 2 for the evaluation of the model (Figure 3a). As can be seen from cross-sectional line profiles of the dried deposits (Figure 3b), the model predicts the number of deposited particles, thus the resulting number of layers very well. However, the CRE formation is not considered in this simple analytical model. Hence, for printing conditions that form a CRE, the prediction may deviate. But minimum dispense velocities or velocity ratios that are required to print lines with a desired number of particle layers can be determined accurately.

As illustrated in the operational phase diagram as well as the line profiles (Figure 3a,b), single line printing was thereby optimal with a particle concentration equal to c = 300 mg mL^{-1}, v_W = 1 mm s^{-1}, and v_D = 23.7 µm s^{-1}. Templates for microfluidic channels as well as the first comb for areas were printed with this parameter set, as explained in the following section.

2.1.2. Printing Layers

To print an entire layer via direct writing, several single lines must be printed that eventually connect and form a dense layer. The common approach is to print several lines consecutively, which we hereby refer to as the "line-by-line" approach. In a recent study by Kim et al.[13] layers were printed via the line-by-line approach, which comprised PhG structures for structural color applications. Differently from here, Kim and coworkers[13] had to add polymers as an additive to increase the suspension's viscosity during printing. In their system, the freshly printed lines spread over time, thus connected eventually with neighboring lines to form a consistent layer. To post-process our

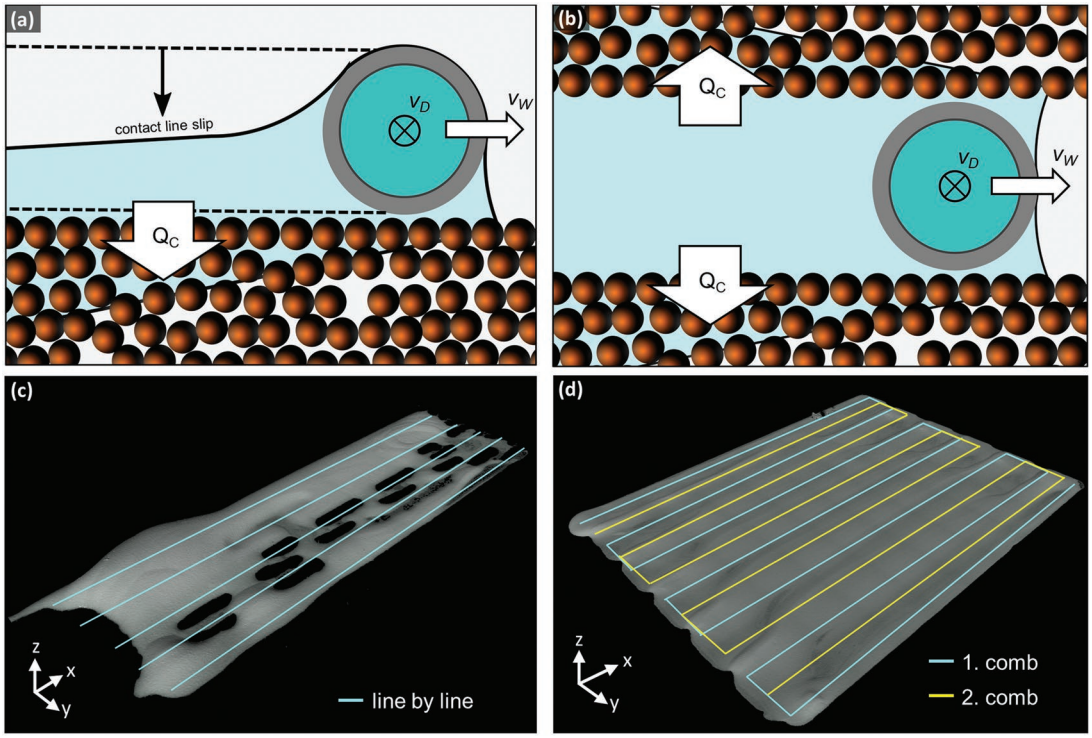

Figure 4. Scheme from top view of a) "line-by-line"-printing and of b) "comb"-printing strategy. 3D view of the topography for the areas printed via c) "line-by-line" and via d) "comb"-strategy: Solid turquoise and yellow lines schematically show printing path for both strategies. Length of printing paths along *x*-direction is ≈8 mm and the distance between lines in y-direction ≈0.6 mm.

templates via ALD, adding such rheology modifiers that would remain in the pores between particles was not an option. However, when printing such low viscous additive-free colloidal suspensions, capillary action disrupts the line-by-line printing strategy. As soon as the wet trailing line connects with the dry neighboring line, the solvent penetrates the previously printed porous particle deposit (**Figure 4**a). This capillary flow Q_c primarily induces an immediate contact line slip, i.e., the outer contact line of the wet trailing line gets dragged toward the previously printed lines due to the capillary forces induced by the porous previously printed layer. Consequently, the liquid bridge becomes unstable forming patchy coatings (Figure 4a,c). When compensating this contact line slip by increasing v_D, the previously printed particle deposits re-disperse, thus forming a secondary CRE during solvent evaporation. The common line-by-line strategy therefore cannot be implemented for direct writing of low viscous additive-free colloidal suspensions.

Instead, we propose a two-step printing approach, the so-called "comb"-strategy. The printing pattern comprises two combs that are printed subsequently (Figure 4b). Both combs are printed with a single stroke, where neighboring line sections are aligned parallel—as with the line-by-line approach—but remain a certain distance to each other. Hence, gaps between line sections of the first comb prevent any contact line slip due to capillary penetration. The first comb may be printed with an arbitrarily shaped silhouette, thereby defining the final shape of the coated area. As soon as the first comb has been printed and dried, a second comb is printed to fill the empty space between neighboring lines of the first comb to form a continuous layer. The liquid bridge and wet trailing line of the second comb penetrates the dried particle deposit of the first comb right away, as expected, but in comparison to the layer-by-layer strategy, on both sides of the wet trailing line (Figure 4b). Therefore, in this case, the capillary penetration can be counterbalanced by the dispense velocity so that the dispense rate $Q_d > Q_c$ and the printing condition can be accurately controlled. To avoid a secondary CRE, due to re-dispersion of the first comb with greater dispense velocities, faster writing velocities v_W can be applied for the second comb (Equation 1), because the first comb fixates the second, thus prevents depinning of the contact line for $v_W > 1$ mm s^{-1}.

When printing areas with the proposed comb strategy, we printed the first comb with the optimized printing parameters for single lines, as described in the previous section. Moreover, the distance between neighboring line sections was reduced such that the gap was consistent but minimal. For an average line width of 0.47 mm we printed line sections with a distance of 0.57 mm, resulting in gaps of ≈100 µm. For smaller distances, neighboring line sections stayed connected at turns of the printing path, thus causing single-sided capillary penetration as for the traditional line-by-line strategy. As shown by the cross-sections of printed areas in **Figure 5**a and mentioned before, high writing velocities are applicable and favored for printing the second comb, because higher v_W reduces A_i (Equation 1). Doubling the writing velocity v_W from 1 to 2 mm s^{-1} reduced the initial cross-section of the wet trailing line by half and prevented the secondary CRE, which is caused

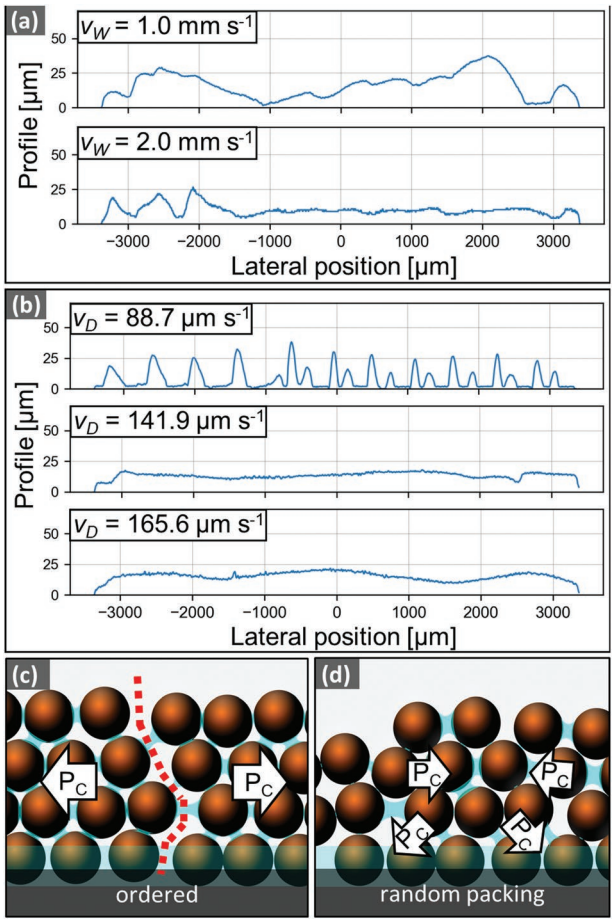

Figure 5. a) Line profiles for areas printed with 1 and 2 mm s^{-1} writing velocity v_W for second comb. Profiles were acquired along transverse axis of main printing direction. b) Transverse line profiles of areas printed with different dispense velocities v_D for second grid (v_D = 37.5, 60.0 and 70.0 µm s^{-1}). Cross-sectional scheme of desiccation process for c) an ordered PS-template forming a crack that is indicated with a red dashed line and for d) an amorphous PS-template that remains crack-free.

by enhanced re-wetting of the first grid for small v_W. However, the PS-template exhibited still regular height fluctuations of up to 20 µm (Figure 5a). To further improve the homogeneity of the layer thickness, the dispense velocity for the second comb was adjusted (Figure 5b). Here, optimizing the dispense velocity v_D for the second comb is a trade-off between too small and too large dispense rates Q_D. If the dispense rate Q_D for the second comb is too small, large height variations in the final deposit form (Figure 5b, v_D = 88.7 µm s^{-1}), since the solvent imbibition creates a capillary flow Q_C, which leads to a CRE in the lines of the second comb (Figure S2, Supporting Information). Printing with too high dispense rates, however, leads to a non-uniform coating as well, due to a secondary CRE induced by re-dispersion of the first comb (Figure 5b, v_D = 165.6 µm s^{-1}). With a dispense velocity v_D = 141.9 µm s^{-1}, we achieved the most homogenous coatings, i.e., the smallest surface undulations (<10 µm for a 7 mm long cross-section). Here, the CRE is minimal, because the dispense rate is high enough, depositing a sufficient amount of particles in the second grid and re-wetting the first comb, thus reducing CRE caused by capillary action in the second comb, but the dispense rate is also small enough to avoid a secondary CRE due to re-dispersion of previously printed particle deposits.

The entire printing process, including solvent evaporation, took less than 10 min for an area of ≈8 × 7 mm. Therefore, this AM process combined with colloidal assembly, forms a fabrication process that is several magnitudes faster than other traditional processes used for colloidal coatings, such as vertical convective self-assembly,[32] which require up to several days for coating of a similar area.[32] In comparison to other faster traditional processes such as drop-cast, where similar areas can be obtained in ≈15–20 min, CRE-free structures are only achieved with additives,[33] pH,[29] or temperature modifications.[30] A recent work by Rey et al.[34] has shown how CRE-free structures can be produced by smart surface-functionalization of the starting particles so that the additive amount is reduced to layers at the particles' surfaces, but no printing was demonstrated. In our approach, we present a strategy to successfully print colloidal structures out of additive-free and low-viscous suspensions. Moreover, due to localized deposition of colloids, which enables printing of submillimeter thin lines and arbitrary shapes, AMCA paths the way for novel applications of colloidal templates. To demonstrate that, the printed PS-templates were subsequently post-processed by ALD to form ceramic microporous structures, which will be described in the following section.

Another important aspect of the printed structures is the absence of cracks (**Figure 6**a and images in Figure S1, Supporting Information). Cracks potentially form in colloidal structures during desiccation.[32] While the solvent is evaporating, the solvent-air interface eventually recedes into the particle deposition,[32] due to capillary bridges formed in between particles that cause a compressive capillary pressure between two neighboring particles.[35] The applied capillary pressure leads to elastic and plastic deformation including particle rearrangement and cracking.[36] When considering a single particle that rearranges during solvent evaporation, the trajectory of the particle's rearrangement depends on the spatial distribution of the capillary bridges on the particle's surface. The particle may be pulled in the direction of the highest density of capillary bridges attached to its surface. A face-centered cubic (FCC) particle assembly potentially forms such high capillary bridge densities, as it exhibits a high particle packing fraction. Therefore, particles next to an FCC-assembly shift presumably toward the crystalline assembly, as the net capillary pressure P_c, exerted by the dense particle packing, pulls them in the corresponding direction (Figure 5c). Such directed particle rearrangements eventually form cracks. In our samples, the PS particles assembled in an entirely amorphous arrangement during printing, even at the bottommost layer. This may be a crucial detail for the most significant feature of the obtained coatings: crack-free over a large area. To the best of our knowledge, these are the largest crack-free colloidal coatings (≈1 cm^2) that have been printed via direct writing so far.[37] Differently from a packing with directional long-range order, the spatial distribution of capillary bridges is assumed random in the amorphous assembly; hence, no net capillary pressure pulls particles in a certain trajectory. Instead, particles may rearrange arbitrarily during

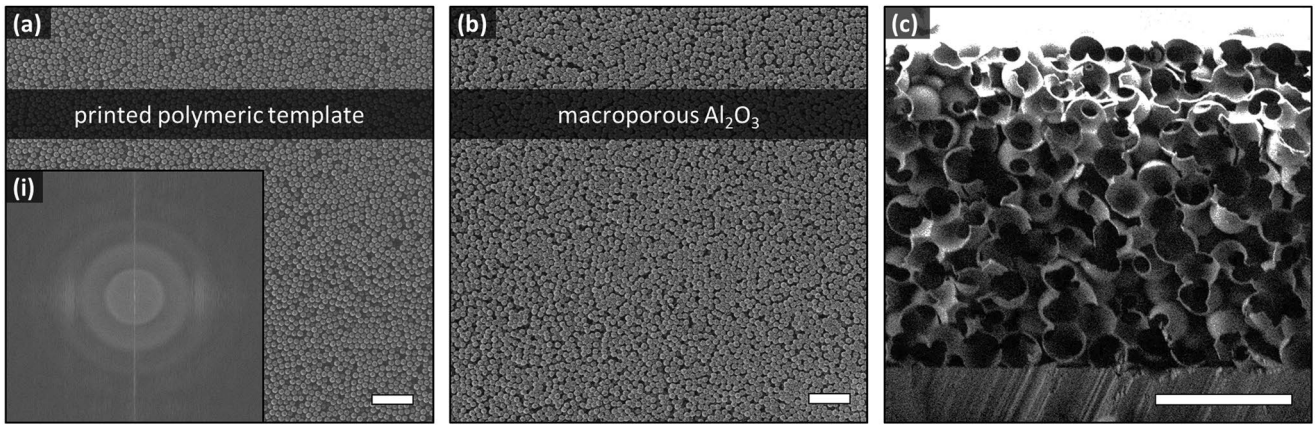

Figure 6. a) SEM image of printed PS-template from top view and a(i)) FFT for SEM image of PS-template. b) SEM image of microporous alumina after coating via ALD and burnout c) cross-section of microporous alumina sample. Scale bars indicate 20 µm (a,b) and 10 µm (c).

solvent evaporation (Figure 5d). Noteworthy, producing such amorphous colloidal coatings has been reported challenging and various strategies have been tested, which include the addition of polymers or monomers to fixate the particles,[37,38] thus preventing crystallization. Here, we achieved an amorphous structure without any additives.

In this study, the fast solvent evaporation induced by the optimization of the printing parameters (<1 min) allows to avoid long-range order and thereby cracks, which is achieved by local suspension deposition during printing. This characteristic of the AMCA process is a unique advantage over other approaches to form macroscopic crack-free colloidal coatings,[32] since it is an additive-free process, with no need for special or patterned substrates, running at room temperature. The absence of cracks in the particle templates is crucial for, e.g., fluid transport or photonic applications, since cracks would form leak boundaries or expose the substrate, when the template is transformed into an inverse structure.[32] In the following, we present demonstrations of these potential applications for our inverted microporous ceramic structures, i.e., microfluidic channels and rTBCs.

2.2. Transforming Printed Particle Templates into Functional Ceramic Structures

The printed polymeric templates were further coated with nanometric thin films to form inverse ceramic structures. Alumina coatings with defined thicknesses (100 and 200 nm) were deposited by ALD and the PS particles were burned out of the coated structures, thereby forming ceramic microporous structures. SEM images of printed areas in top view reveal a densely packed amorphous particle assembly (Figure 6a,b). A fast Fourier transform (FFT) of the SEM image does not contain any clear peaks, but a circular ring pattern thus demonstrates the short-range order and confirms the amorphous state of the particle assembly (Figure 6a(i)). The amorphous assembly is retained after ALD and polymer burn-out, as shown by the cross-section of the ceramic structure after calcination: Micropores were randomly distributed over the entire cross-section (Figure 6c).

2.2.1. Microfluidic Channels

Single printed lines, here a "TUHH" logo (**Figure 7**a), were transformed into microporous channels via ALD and calcination possessing a wall thickness of 100 nm, as described in the section above. After ALD, the channels were cut open to enable penetration of the liquid within the porous ceramic network. When placing an aqueous methylene blue droplet next to a channel opening, the fluid penetrated the channel due to capillary action. The as-produced alumina channels exhibited high permeability, i.e., the "T" and "H" channels were wetted by the fluid entirely (Figure 7a). It further demonstrates the importance to produce crack-free structures, as the presence of cracks would likely lead to fluid leakage and spill out of the letters' boundary. Curiously, the "U" channel was not entirely wetted

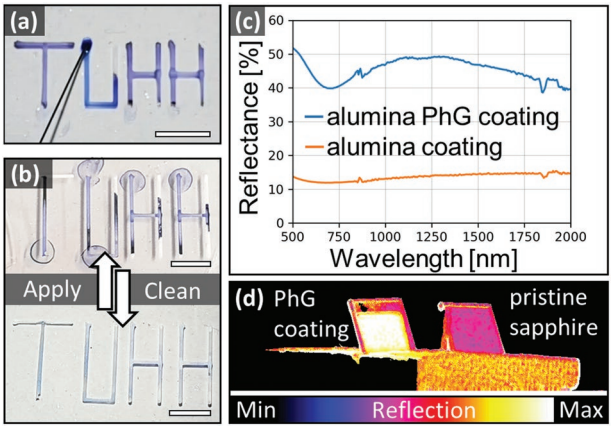

Figure 7. a) Photograph of "TUHH"-microporous alumina sample. The interconnected micropores within the channels transport aqueous methylene blue solution that is dispensed at the inlet of the ceramic channels. b) Photographs of a TUHH-sample (33% larger than sample in (a)) after (top) a methylene blue experiment and after (bottom) 24 h immersion in water for cleaning. The microporous channels can be reused. Scale bars represent 5 mm. c) VIS-NIR reflectance measurement of PhG coating on sapphire and flat alumina coating on sapphire. d) False color image from IR camera measuring reflected heat radiation on the surface of the PhG coating and a pristine sapphire. The bar in the bottom elucidates the color code for the intensity of the reflected heat radiation.

with the methylene blue solution. Here, a maximum penetration length of ≈12 mm was achieved within 17 s (Figure 7a). We associate the incomplete wetting of the "U" channel to the greater length of the channel from entrance to exit, which eventually exceeded the transport capability of the microporous ceramic structure. Further dedicated fluid-transport studies are planned to elucidate and model the relation between the structural parameters and transport capabilities of these inverse microporous ceramic structures.

To evaluate the wicking capability of our produced microporous channels, the capillary performance parameter K/R_{eff} was assessed by:[39,40] $K/R_{eff} = \mu h^2 f/4\sigma t$, where K is the permeability, R_{eff} is the effective pore radius, μ is the dynamic viscosity of the fluid, h is the penetration length, σ is the surface tension of the fluid and t is the penetration time. Assuming a packing fraction of 0.64 for the amorphous packing,[31] our alumina channels obtained a capillary performance K/R_{eff} = 0.017 µm. Therefore, our ceramic channels with nanosized walls demonstrated a remarkable capillary performance, considering K/R_{eff} being reported between 0.001–0.023 µm in the literature for copper inverse opals[39,41] and copper nanowire arrays.[40]

In future, the capillary performance of our microfluidic channels could be further enhanced by tuning the processing parameters. Here, both the AMCA and ALD process allow for precise control of the structural parameters in the ceramic structures. Moreover, the printing process enables easy fabrication of arbitrary channel paths, while the ceramic structure assures mechanically and chemically robust channels. Rinsing as well as immersion in distilled water for up to 24 h did not affect the channels' integrity (Figure 7b). Hence the channels could potentially be recycled and reused upon development of a cleaning treatment. To date, mainly polymer-based microfluidic channels are produced, e.g., via soft lithography.[5] With the presented process route; however, microfluidic channels can be produced from various ceramics. This paves the way to novel applications of microfluidics in so far rather inapplicable environments, i.e., corrosive or high-temperature environments. For instance, ceramic microporous channels could potentially be utilized as microfluidic cooling devices for heat management on high-power electronics in aerospace platforms.[4]

2.2.2. Photonic Coatings

The printed PS-template areas were transformed into ceramic microporous coatings, to demonstrate the potential application as rTBCs. The amorphous assembly of monodisperse particles and subsequent ALD coating followed by calcination results in an inverse PhG structure. This class of photonic materials, PhG, possesses a broadband reflection capability that is angular independent and can be tailored by adjusting the effective refractive index of the ceramic structure as well as the pore size.[7]

Our ceramic inverse PhG structure demonstrated such remarkable broadband reflection in the near-infrared (NIR) region as visualized in the UV–vis–NIR reflectance measurements (Figure 7c). While the flat non-structured alumina coating on sapphire shows an almost constant reflectance of maximum 15 %, the alumina PhG enhances the reflection up to 50 % in the 500–2000 nm wavelength range. Diffuse reflection but also specular reflection were assessed with the integrating sphere setup. Hence, the 15% reflectance achieved with the flat alumina coating on the sapphire substrate can be correlated to specular reflection. The remarkable increase in reflectance for the ceramic PhG gives additional evidence for an amorphous pore network. In comparison, a photonic crystal would show a narrow peak in the spectrum.[42] To increase the reflectance of the coating further, greater wall-thicknesses of the PhG or the coating of a ceramic material possessing a higher refractive index could be used to additionally increase the material volume fraction and effective refractive index of the structure, respectively.[43] Here, alumina with a refractive index of 1.7 (at a wavelength of 633 nm) and 200 nm of film thickness was used as proof of principle.

To additionally visualize the reflection capabilities of our coatings, we placed the alumina inverse PhG coating as well as a pristine sapphire substrate in front of an oven that was heated to 1000 °C. The heat radiation that was emitted from the oven and reflected from the sample surfaces was captured with an IR-camera and is shown in Figure 7d. The sample surfaces were oriented such that diffuse reflection was mainly acquired. The 20 µm thin photonic coating, demonstrated the highest reflection intensity (Figure 7d), which was even higher than the reflection from the alumina refractory bulk porous ceramic block that was primarily used as mounting for the samples (50 × 30 × 10 mm). This demonstrates the great potential of such inverse PhG ceramic coatings, which could potentially be applied as next- generation rTBCs in high-temperature applications.[7] Here, AMCA also offers an advantage as it enables the coating of inclined, curved and complex surfaces in 3D.[9]

3. Conclusion

This work established groundbreaking guidelines for the direct writing of low viscous colloidal suspensions. We demonstrated the printing of uniform, crack-free, macroscale templates of arbitrary shape made of monodisperse PS microparticles for subsequent transformation into ceramic microporous structures for different applications. We showed that the CRE can be prevented in single lines by increasing the velocity ratio v_W/v_D, while the particle concentration in the suspension must be above a minimum concentration to maintain self-pinning of the contact line during printing. Above this threshold, the concentration can be tailored for a desired number of particle layers in the final deposit. For printing areas, we demonstrated that the common line-by-line approach is not suitable for additive-free low viscous colloidal suspensions, thus we introduced a novel "comb"-strategy to circumvent the hurdles of capillary penetration, thereby enabling printing of macroscopic uniform areas within short processing times and without requiring further additives. We used ALD to transform the printed templates into functional ceramic structures, demonstrating possible applications of such in microfluidics and high-temperature applications. Remarkable wicking capabilities and broadband reflection in NIR of the attained structures highlight the great potential of the AMCA process combined with ALD functionalization, which establishes novel macroscopic applications for colloidal-based structures.

4. Experimental Section

Additive Manufacturing Combined with Colloidal Assembly: Aqueous monodispersePS suspensions with a particle radius R_P of 1.5 µm (SD = 0.09 µm, Microparticles GmbH) were printed on sapphire substrates (0.53 mm thick sheets cut along A-plane, Crystec GmbH) with a custom-made direct writing equipment. The PS solid particle concentration of the as-delivered suspension was 100 mg mL^{-1}, being varied for the study (50, 100, 150, 200, 250, 300, and 350 mg mL^{-1}) in order to determine the best parameters for printing. To increase the concentration, the suspension was centrifuged and the supernatant was pipetted out of the suspension. The colloidal suspension was stabilized electrostatically as the zeta-potential of –31.9 ± 0.7 mV (pH 5.76) demonstrated. Syringes with a 25 µL barrel volume (1702 RN, Hamilton Company) and PTFE-coated needles with an inner- and outer diameter of 0.127 and 0.474 mm were used for printing. The suspensions were sonicated for 10 min, prior to filling the syringes. Three linear stages moved the substrate beneath the needle tip during printing. A fourth one was connected to the plunger of the syringe to dispense the suspension with a specific dispense velocity (M-126.2S1, Physics Instruments). For printing single lines and areas, macros were written with GCS command set (Mercury GCS Commands, Physics Instruments) and executed with the supplied software.

Atomic Layer Deposition: ALD was used to coat the printed structure with thin films of aluminum oxide at 95 °C using nitrogen as carrier gas (15 sccm) in a custom-made reactor (Hamburg University of Technology, TUHH) under exposure modus. The precursors used were Trimethylaluminium (TMA, Sigma–Aldrich) and deionized water. The thickness and refractive index of the resulting films were measured by spectroscopic ellipsometry (SENProTM, SENTECH Instruments GmbH) in films deposited on reference silicon wafers placed within the reactor close to the 3D printed structures.

The average resulting growth per cycle (GPC) was 1.8 Å for aluminum oxide. To generate the ceramic microporous structures, the polymeric core was removed by burn-out in air for 30 min with a heating rate of 0.8 °C min^{-1} from room temperature up to 500 °C.

Characterization: The printing process was monitored using a CMOS camera (EO-10012C ½" CMOS, Edmund Optics) with a 5× optical magnification lens. The camera was placed next to the sample stage to monitor the process in side view. Temperature as well as humidity were tracked during sample preparation. Both varied slightly from 22–23 °C and 19–27%, respectively.

To investigate the lateral particle distribution in printed single lines, height profiles of printed single lines were attained with the DektakXT profilometer by Bruker. A stylus with radius of 2 µm (B-Type) was used and the following measurement parameters were applied: scan range of 65.5 µm, standard scan type, profile type "Hills & Valleys" and a stylus force of 1 mg. A scan resolution of ≈0.2 µm pt^{-1} was kept constant for all measurements. The topography of printed areas was scanned with an optical surface metrology instrument (Alicona G4 Infinite Focus). A 10× optical magnification lens was used resulting in a vertical resolution of 0.1 µm. The particle ordering of the deposits was analyzed with a scanning electron microscope (Zeiss Supra VP55) using a low voltage of 1.5 kV and a working distance of ≈5 mm.

The microfluidic transport (wicking) capabilities of the produced ceramic channels were investigated by recording the capillary flow of an aqueous 5 mg mL^{-1} methylene blue solution. The channels were cut open on two ends to allow penetration of the microporous structure. A sessile droplet of the methylene blue solution was placed at one open channel site and the capillary fluid transport was recorded in top view for subsequent determination of the capillary performance parameter K/R_{eff}.[41]

A UV–vis-NIR spectrophotometer (Lambda 1050, Perkin Elmer) and integrating sphere accessory were used to measure diffuse reflectance spectra of the fabricated inverse PhG coatings in the visible to NIR (0.5–2 µm). Moreover, the capability to reflect heat radiation was visualized with an infrared camera (HDRC -Quotienten-PyroCam, IMS Chips Stuttgart) by monitoring the surface of the coatings that was exposed to a 1000 °C hot furnace as radiation source. The samples' surfaces were inclined to the heat source and the infrared camera was placed perpendicular to the furnace such that diffuse reflection of the heat radiation on the samples' surfaces could be captured but no radiation reached the camera directly from the heat source. A thermocouple was placed between the two substrates, measuring the ambient temperature at the samples position, which was constant at 100 °C. Therefore, the reflected heat radiation at the sample surfaces could be visualized with a false color image, because both, the emitted radiant power from the samples as well as transmitted radiant power from the surroundings were small (100 °C) in comparison to the reflected radiant power from the oven (1000 °C).

Supporting Information

Supporting Information is available from the Wiley Online Library or from the author.

Acknowledgements

The authors gratefully acknowledge the financial support from the Deutsche Forschungsgemeinschaft (DFG, German Research Foundation) – Projektnummer 192346071 – SFB 986, project C4. The authors thank Stephanie Haugg and Prof. Robert Blick from the Center for Hybrid Nanostructures in the University of Hamburg for providing training and access to the profilometer, respectively.

Open access funding enabled and organized by Projekt DEAL.

Conflict of Interest

The authors declare no conflict of interest.

Data Availability Statement

The data that support the findings of this study are available from the corresponding author upon reasonable request.

Keywords

additive manufacturing, coffee ring effect, colloids, crack-free structures, microfluidics, photonic structures, self-assembly

Received: September 9, 2022
Revised: November 11, 2022
Published online:

[1] J. Liu, V. Nguyen-Van, B. Panda, K. Fox, A. Du Plessis, P. Tran, *3D Print. Addit. Manuf.* **2022**, *9*, 12.
[2] M. Salmi, *Materials* **2021**, *14*, 191.
[3] B. Blakey-Milner, P. Gradl, G. Snedden, M. Brooks, J. Pitot, E. Lopez, M. Leary, F. Berto, A. Du Plessis, *Mater. Des.* **2021**, *209*, 110008.
[4] M. T. Barako, V. Gambin, J. Tice, *Nanotechnology* **2018**, *29*, 154003.
[5] K. Y. Suh, S. M. Kim, S. H. Lee, M. C. Park, K. W. Kwon, P. Kim, *Bio-Chip J.* **2008**, *2*, 1.
[6] G. Shang, P. Dyachenko, E. W. Leib, T. Vossmeyer, A. Petrov, M. Eich, *Ceram. Int.* **2020**, *46*, 19241.
[7] J. J. do Rosário, Y. Häntsch, R. M. Pasquarelli, P. N. Dyachenko, E. Vriend, A. Y. Petrov, K. P. Furlan, M. Eich, G. A. Schneider, *J. Eur. Ceram. Soc.* **2019**, *39*, 3353.

[8] Z. Faraji Rad, P. D. Prewett, G. J. Davies, *Microsyst. Nanoeng.* **2021**, *7*, 71.
[9] B. F. Winhard, S. Haugg, R. Blick, G. A. Schneider, K. P. Furlan, *J. Colloid Interface Sci.* **2021**, *597*, 137.
[10] a) J. Hou, M. Li, Y. Song, *Angew. Chem., Int. Ed.* **2018**, *57*, 2544; b) M. Liu, J. Wang, M. He, L. Wang, F. Li, L. Jiang, Y. Song, *ACS Appl. Mater. Interfaces* **2014**, *6*, 13344; c) W. Shen, M. Li, C. Ye, L. Jiang, Y. Song, *Lab Chip* **2012**, *12*, 3089.
[11] A. Demiroers, E. Poloni, M. Chiesa, F. Bargardi, M. Binelli, W. Woigk, L. de Castro, N. Kleger, A. Studart, *3D Printing of Photonic Colloidal Glasses into Objects with Isotropic Structural Color*, Research Square Platform LLC, Durham, NC **2022**.
[12] B. Domènech, A. T. L. Tan, H. Jelitto, E. Zegarra Berodt, M. Blankenburg, O. Focke, J. Cann, C. Cem Tasan, L. Colombi Ciacchi, M. Müller, K. P. Furlan, A. John Hart, G. A. Schneider, *Adv. Eng. Mater.* **2020**, *22*, 2000352.
[13] J. B. Kim, C. Chae, S. H. Han, S. Y. Lee, S.-H. Kim, *Sci. Adv.* **2021**, *7*, 8780.
[14] A. T. L. Tan, J. Beroz, M. Kolle, A. J. Hart, *Adv. Mater.* **2018**, *30*, 1803620.
[15] A. T. L. Tan, S. Nagelberg, E. Chang-Davidson, J. Tan, J. K. W. Yang, M. Kolle, A. J. Hart, *Small* **2020**, *16*, 1905519.
[16] R. D. Deegan, O. Bakajin, T. F. Dupont, G. Huber, S. R. Nagel, T. A. Witten, *Nature* **1997**, *389*, 827.
[17] P. C. Duineveld, *J. Fluid Mech.* **2003**, *477*, 175.
[18] Y. Jiang, S. Hu, Y. Pan, *3D Print. Addit. Manuf.* **2018**, *5*, 301.
[19] a) S. Schiaffino, A. A. Sonin, *J. Fluid Mech.* **1997**, *343*, 95; b) J. Stringer, B. Derby, *Langmuir* **2010**, *26*, 10365.
[20] Á. G. Marín, H. Gelderblom, D. Lohse, J. H. Snoeijer, *Phys. Rev. Lett.* **2011**, *107*, 85502.
[21] N. D. Patil, R. Bhardwaj, A. Sharma, *Langmuir* **2018**, *34*, 12058.
[22] J.-y. Jung, Y. W. Kim, J. Y. Yoo, J. Koo, Y. T. Kang, *Anal. Chem.* **2010**, *82*, 784.
[23] Y.-S. Yu, X.-L. Xia, X. Zheng, X. Huang, J.-Z. Zhou, *Sci. China: Phys., Mech. Astron.* **2017**, *9*, 60.
[24] Y.-S. Yu, M.-C. Wang, X. Huang, *Sci. Rep.* **2017**, *7*, 14118.
[25] *Capillarity and Wetting Phenomena. Drops, Bubbles, Pearls, Waves*, (Eds. P.-G. deGennes, F. Brochard-Wyart, D. Quéré), Springer, New York, **2004**.
[26] X. Shen, C.-M. Ho, T.-S. Wong, *J. Phys. Chem. B* **2010**, *114*, 5269.
[27] T. Still, P. J. Yunker, A. G. Yodh, *Langmuir* **2012**, *28*, 4984.
[28] H.-Y. Ko, J. Park, H. Shin, J. Moon, *Chem. Mater.* **2004**, *16*, 4212.
[29] R. Bhardwaj, X. Fang, P. Somasundaran, D. Attinger, *Langmuir* **2010**, *26*, 7833.
[30] Y. Li, Q. Yang, M. Li, Y. Song, *Sci. Rep.* **2016**, *6*, 24628.
[31] G. D. Scott, D. M. Kilgour, *J. Phys. D: Appl. Phys.* **1969**, *2*, 863.
[32] Z. Jiang, Z. Hsain, J. H. Pikul, *Langmuir* **2020**, *36*, 7315.
[33] M. Anyfantakis, Z. Geng, M. Morel, S. Rudiuk, D. Baigl, *Langmuir* **2015**, *31*, 4113.
[34] M. Rey, J. Walter, J. Harrer, C. M. Perez, S. Chiera, S. Nair, M. Ickler, A. Fuchs, M. Michaud, M. J. Uttinger, A. B. Schofield, J. H. J. Thijssen, M. Distaso, W. Peukert, N. Voge, *Nat. Commun.* **2022**, *13*, 2840.
[35] M. Schneider, J. Maurath, S. B. Fischer, M. Weiß, N. Willenbacher, E. Koos, *ACS Appl. Mater. Interfaces* **2017**, *9*, 11095.
[36] L. Goehring, W. J. Clegg, A. F. Routh, *Phys. Rev. Lett.* **2013**, *110*, 24301.
[37] Y. Hu‡, Y. Zhang‡, D. Yang, D. Ma, S. Huang, *Mater. Adv.* **2021**, *2*, 6499.
[38] Y. Hu, D. Yang, S. Huang, *ACS Omega* **2019**, *4*, 18771.
[39] Q. N. Pham, M. T. Barako, J. Tice, Y. Won, *Sci. Rep.* **2017**, *7*, 10465.
[40] J. Lee, Y. Suh, P. P. Dubey, M. T. Barako, Y. Won, *ACS Appl. Mater. Interfaces* **2019**, *11*, 1546.
[41] Q. N. Pham, B. Shao, Y. Kim, Y. Won, *ACS Appl. Mater. Interfaces* **2018**, *10*, 16015.
[42] a) Z. Cai, Y. J. Liu, J. Teng, X. Lu, *ACS Appl. Mater. Interfaces* **2012**, *4*, 5562; b) D.-K. Hwang, H. Noh, H. Cao, R. P. H. Chang, *Appl. Phys. Lett.* **2009**, *95*, 091101.
[43] J. J. do Rosário, P. N. Dyachenko, R. Kubrin, R. M. Pasquarelli, A. Y. Petrov, M. Eich, G. A. Schneider, *ACS Appl. Mater. Interfaces* **2014**, *6*, 12335.